JCB

Article

SPR2 protects minus ends to promote severing and reorientation of plant cortical microtubule arrays

Masayoshi Nakamura,[1]* Jelmer J. Lindeboom,[1]* Marco Saltini,[2] Bela M. Mulder,[2,3] and David W. Ehrhardt[1,4]

[1]Department of Plant Biology, Carnegie Institution for Science, Stanford, CA
[2]Institute AMOLF, Amsterdam, Netherlands
[3]Laboratory of Cell Biology, Wageningen University, Wageningen, Netherlands
[4]Department of Biology, Stanford University, Stanford, CA

The cortical microtubule arrays of higher plants are organized without centrosomes and feature treadmilling polymers that are dynamic at both ends. The control of polymer end stability is fundamental for the assembly and organization of cytoskeletal arrays, yet relatively little is understood about how microtubule minus ends are controlled in acentrosomal microtubule arrays, and no factors have been identified that act at the treadmilling minus ends in higher plants. Here, we identify *Arabidopsis thaliana* SPIRAL2 (SPR2) as a protein that tracks minus ends and protects them against subunit loss. SPR2 function is required to facilitate the rapid reorientation of plant cortical arrays as stimulated by light perception, a process that is driven by microtubule severing to create a new population of microtubules. Quantitative live-cell imaging and computer simulations reveal that minus protection by SPR2 acts by an unexpected mechanism to promote the lifetime of potential SPR2 severing sites, increasing the likelihood of severing and thus the rapid amplification of the new microtubule array.

Introduction

The interphase microtubule (MT) arrays of higher plants are essential to create plant cell and tissue shape, a role they perform in part by guiding patterns of cell wall biosynthesis (Cyr, 1994; Baskin, 2005; Paradez et al., 2006; Oda, 2015). To carry out this function, interphase MTs are located at the cell cortex in association with the cell membrane, where they acquire specific and highly ordered architectures that are dynamically responsive to environmental and hormonal signals. These cortical arrays are built and reorganized without a centrosomal organizer to position and regulate polymer nucleation. Instead, interphase nucleation is distributed along the sides of existing MTs, where new polymers are initiated either in parallel to the mother MT or at a branching angle (Murata et al., 2005; Chan et al., 2009; Nakamura et al., 2010). These nascent MTs are subsequently separated from their nucleation complexes by katanin-mediated severing (Nakamura and Hashimoto, 2009; Nakamura et al., 2010), yielding free minus ends and generating highly dynamic arrays of treadmilling polymers (Shaw et al., 2003). Although higher plant cells lack centrosomes altogether, many differentiated animal cells also assemble interphase arrays without centrosomal participation. How such acentrosomal arrays are built and reorganized to carry out specialized cellular functions are central questions in cell biology.

A defining feature of the acentrosomal cortical arrays of higher plants is that both polymer ends are dynamic. Although the assembly and dynamics of plus ends and their control by associated binding factors (+TIPs) have been subjects of intense study, relatively little is known about the cellular factors that control minus end stability and dynamics once MTs are detached from their nucleation complexes. Recent studies have identified CAMSAP/Patronin/Nezha family proteins in human and insect cells that protect MT minus ends from depolymerization independently of γ-tubulin (−TIPs; Akhmanova and Steinmetz, 2015). Despite the presence of pervasive free minus ends, no proteins to date have been identified that modulate the stability and dynamics of free minus ends in higher plants. Further, the functional consequences of failing to modulate minus-end dynamics appropriately have not been investigated. Here, we present evidence that the *Arabidopsis thaliana* SPIRAL2 (SPR2) protein localizes to and tracks minus ends of interphase MTs, where it protects these ends from rapid depolymerization. We show that this activity is required to facilitate dynamic remodeling of the cortical array as stimulated by the perception of blue light, a process that rapidly builds a new population of MTs by katanin-mediated severing at MT crossovers (Lindeboom et al., 2013; Nakamura, 2015). Quantitative analysis of MT dynamics and severing at crossovers, together with

---

*M. Nakamura and J.J. Lindeboom contributed equally to this paper.

Correspondence to David Ehrhardt: ehrhardt@stanford.edu

M. Nakamura's present address is Institute of Transformative Bio-Molecules, Nagoya University, Nagoya, Japan.

Supplemental material can be found at:
http://doi.org/10.1083/jcb.201708130

The Rockefeller University Press
J. Cell Biol.
https://doi.org/10.1083/jcb.201708130

computational modeling, indicates that SPR2 acts to increase the likelihood of severing at crossovers by promoting the opportunity time for severing.

Results

SPR2 accumulates at and tracks dynamic minus ends

SPR2/TORTIFOLIA1 was originally identified by recessive mutations in *Arabidopsis* that confer prominent right-handed (viewed from above) twisting in leaf petioles and flower petals (Furutani et al., 2000; Buschmann et al., 2004; Shoji et al., 2004). Fluorescent protein fusions to the SPR2 protein (Yao et al., 2008; Wightman et al., 2013), revealed a complex pattern of localization dependent on the MT cytoskeleton. Dynamic foci were visible in these datasets with patterns of label accumulation that were consistent with growing MT plus ends (Yao et al., 2008) and at sites where MTs intersect and crossover (Wightman et al., 2013). To assess the relationship between the SPR2 signal and MT behavior more directly, we created transgenic lines that coexpress SPR2-GFP from a native upstream sequence (Yao et al., 2008) together with the MT marker mCherry-TUA5 as driven from a constitutive promoter (Gutierrez et al., 2009). The SPR2-GFP construct was previously shown to complement function of the *spr2-2* loss-of-function mutant (Yao et al., 2008). We observed moderate SPR2-GFP labeling along the MT lattice in dark grown epidermal hypocotyl cells, together with accumulation at growing, but not shrinking, plus ends and at crossovers (Fig. 1, A–E; Fig. S1; and Video 1) as previously reported (Yao et al., 2008; Wightman et al., 2013). However, we also detected a population of distinct and prominent foci that clearly localized to and tracked the minus ends of MTs (Fig. 1, A–E; Fig. S1; and Videos 2 and 3). Interestingly, Yao et al. (2008) reported that minus-end dynamics were affected by the addition of SPR2 protein in vitro, although no observation of minus end localization was possible in that study because of use of unlabeled SPR2 protein.

To quantify the relative accumulation of SPR2-GFP at dynamic minus ends, plus ends, MT crossovers, and the general MT lattice, we first identified branching MT nucleation events in image times series taken at the cell cortex in dark grown hypocotyl cells (Fig. 1, A and B; and Videos 2 and 3). Newly nucleated MTs are typically detached from their birth sites by katanin-mediated severing, producing a free and dynamic minus end (Murata et al., 2005; Nakamura et al., 2010). Thus, observation of nucleation allows for robust identification of both plus and minus ends. Locations were selected for measurement of SPR2-GFP and mCherry-TUA5 signal corresponding to minus ends, plus ends, sites where the nucleated MT crossed over other MTs, and sites along the general MT lattice. To avoid possible observer bias arising from the distribution of SPR2 signal, both the branching nucleation events and the locations for measurement were selected in the MT channel before examining the SPR2 channel. The relative SPR2 signal was calculated as SPR2 signal divided by the sum of the SPR2 signal and the MT signal. These measurements confirmed the accumulation of SPR2 signal at minus ends, plus ends, and crossovers over that on the general MT lattice and revealed that the relative SPR2 signal levels at plus ends, minus ends, and crossovers were similar (Fig. 1 E).

We used the same sample of branching nucleation events described in the previous paragraph to quantify the distribution of SPR2-GFP signal relative to free minus ends. Once each free minus end was resolved from the mother MT by formation of an optically resolved gap, the signal was measured in both channels along a transect line that spanned the minus end, and the signal profiles were aligned by the position of signal edge in the MT channel. The mean signal profiles are shown in Fig. 1 F, indicating an ~4.75-fold peak enrichment of SPR2-GFP at the minus end tips as compared with that on the adjacent lattice.

The prevalence of SPR2-GFP enrichment at free minus ends was assessed by examining populations of minus ends created by severing. Severing in *Arabidopsis* cortical arrays occurs both at nucleation sites and at locations where cortical MTs intersect and crossover each other (Lindeboom et al., 2013; Wightman et al., 2013; Zhang et al., 2013). In both cases, free minus ends were first identified by information in the MT channel only, and then SPR2-GFP localization was examined. At nucleation sites, kymograph analysis revealed that all observed minus ends generated by severing (28 of 28) showed accumulation and tracking over time by SPR2-GFP (Fig. 1, A and B; and Video 2). Interestingly, accumulation of SPR2-GFP signal was typically not observed at the branching site when new MT growth was first detected (Fig. 1, A and B), suggesting that SPR2 protein may not be recruited to the minus end when it is still associated with the nucleation complex. At crossovers, and in the general population of free and dynamic ends, plus and minus ends can be identified from assessment of their dynamic behavior; plus ends in *Arabidopsis* cortical arrays feature dynamic instability characterized by episodes of rapid growth and loss, whereas minus ends show primarily pause and slow loss, with no episodes of rapid growth (Shaw et al., 2003; Materials and methods). Crossovers are therefore created by growth of a plus end and observation of crossover formation allows the polarities of the new ends generated by severing of that MT to be known. SPR2-GFP signal was observed to accumulate at and to track 71 of 71 new minus ends created by severing at crossovers (Fig. 1, C and D; and Video 4). Collectively, our experimental data reveal SPR2 to be a pervasive and persistent marker of free MT minus ends in the interphase cortical arrays of *Arabidopsis* hypocotyl cells, whether created by severing from nucleation sites or at MT crossovers.

SPR2 regulates dynamics of minus ends

The minus-end tracking activity of SPR2-GFP, together with the observation that SPR2 affects minus-end dynamics in vitro (Yao et al., 2008), suggested that SPR2 could have a function in controlling minus-end dynamics in vivo. To test this hypothesis, we measured cortical MT dynamics in dark-grown hypocotyl cells expressing mCherry-TUA5 in both WT and the *spr2-2* loss-of-function mutant (Fig. 2, A and B). Minus and plus ends were identified by their distinct dynamics, with the ability or lack of ability to show rapid growth being a robust determinant of plus or minus end identity, respectively (Materials and methods). Quantification of minus-end dynamics (Materials and methods) showed that the mean shrinking speed was 2.74-fold higher (Fig. 2 C; 3.45 µm/min in *spr2-2* and 1.26 µm/min in WT; $P < 0.001$, Mann–Whitney *U* test). Further, we found that the transition rate of minus-end pausing to shrinking (r_{ps}) was significantly increased in *spr2-2* compared with WT ($P < 0.001$, rate ratio test), and at the same time, the transition rate of shrinking to pausing (r_{sp}) was significantly decreased in *spr2-2* compared with WT (Fig. 2 D;

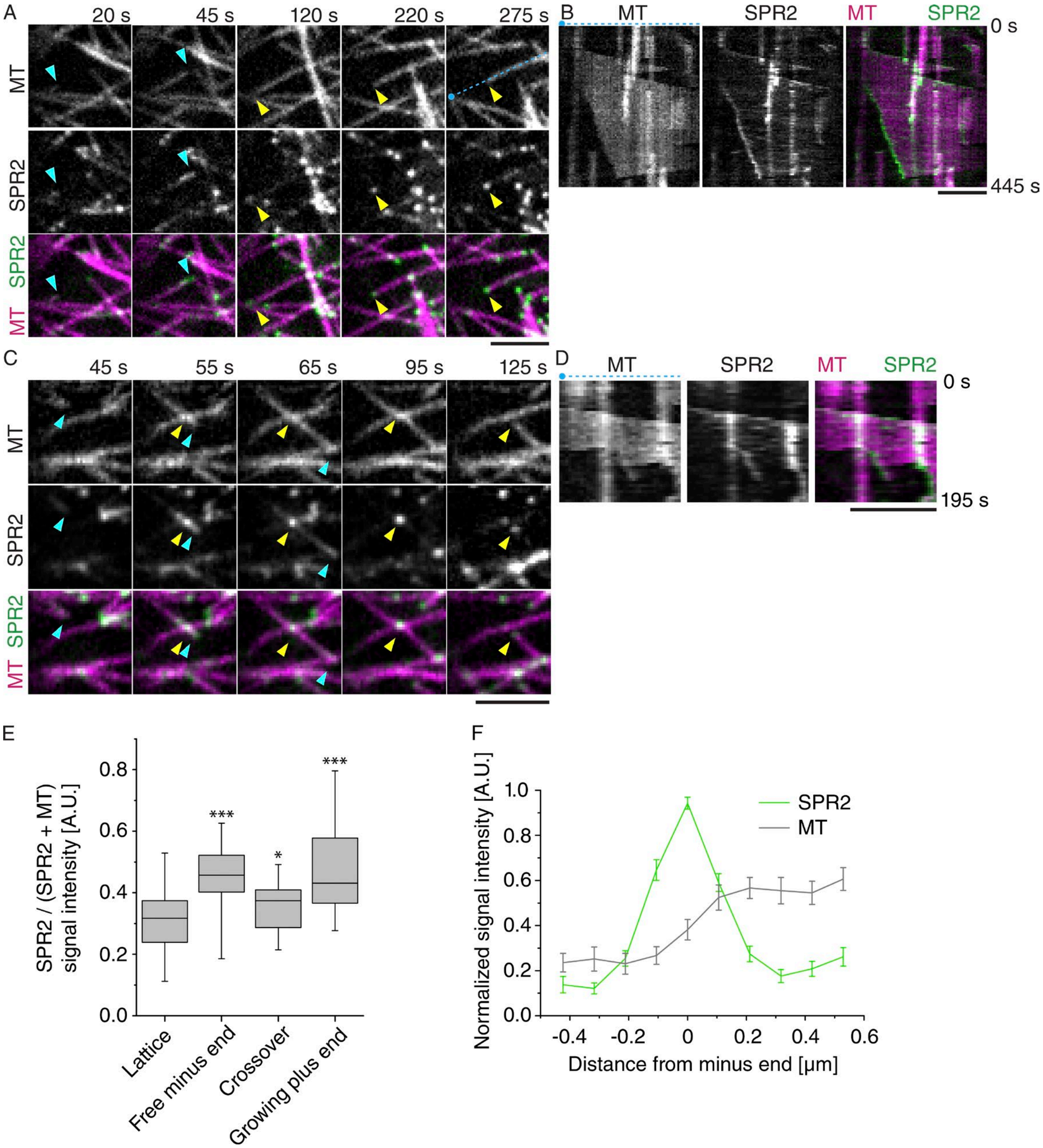

Figure 1. **SPR2 is recruited to MT minus ends. (A)** Representative confocal time-lapse images of an MT nucleation event showing SPR2-GFP (SPR2) signal and a single MT labeled by mCherry-TUA5 (MT). Blue and yellow arrowheads indicate plus-end and minus-end localization of SPR2, respectively. **(B)** Kymographs generated from images in A (at the blue dotted line) showing the dynamics of the SPR2 and MT label over time. **(C)** Example time-lapse images of MT and SPR2 signal localization at an MT crossover and at the MT minus end after MT severing at that crossover. Yellow arrowheads indicate SPR2 foci on an MT crossover followed by localization at a depolymerizing MT minus end after severing at that crossover site. Blue arrowheads indicate a growing MT plus end. **(D)** Kymographs generated from images in C (at the blue dotted line). **(E)** Relative SPR2-to-MT signal intensities at the MT lattice (*n* = 28), free minus ends (*n* = 27), crossovers (*n* = 23), and growing plus ends (*n* = 28) after MT nucleation. Asterisks indicate a significant difference in signal compared with that at MT lattice (Mann–Whitney *U* test; *, P < 0.05; ***, P < 0.001). **(F)** Normalized SPR2 and MT (MT) signal intensities at the MT minus end. The MT signal shows the edge of the minus end signal at position 0, a location where we measure a peak in SPR2 signal that is significantly higher than that on the MT lattice (see positions 0.2 μM and greater). *n* = 28; error bars indicate SEM. Bars, 3 μm.

$P < 0.001$, rate ratio test). The increase in r_{ps} and decrease in r_{sp} in the *spr2-2* mutant resulted in an increase in the fraction of time that the minus ends are shrinking instead of pausing, from 65% in WT to 9% in *spr2-2* (Fig. 2 E). Thus, minus ends shrink faster and spend more time shrinking in the *spr2-2* mutant, making free minus ends much less stable than those in WT.

To ask whether SPR2 is a ubiquitous minus-end stabilizing factor, we quantified the velocity of ends that were generated by laser dissection (Magidson et al., 2007). In cells WT for SPR2, both new ends created by severing were observed to shrink immediately. One end of each pair showed accumulation of SPR2-GFP within 6 s of laser ablation, whereas the other end did not (Fig. 3 A and Video 5; 36 severed MTs observed). Because SPR2-GFP labeled all shrinking minus ends generated by severing at nucleation sites and at crossovers, the labeled ends were thus likely to be the minus ends (note that SPR2-GFP was

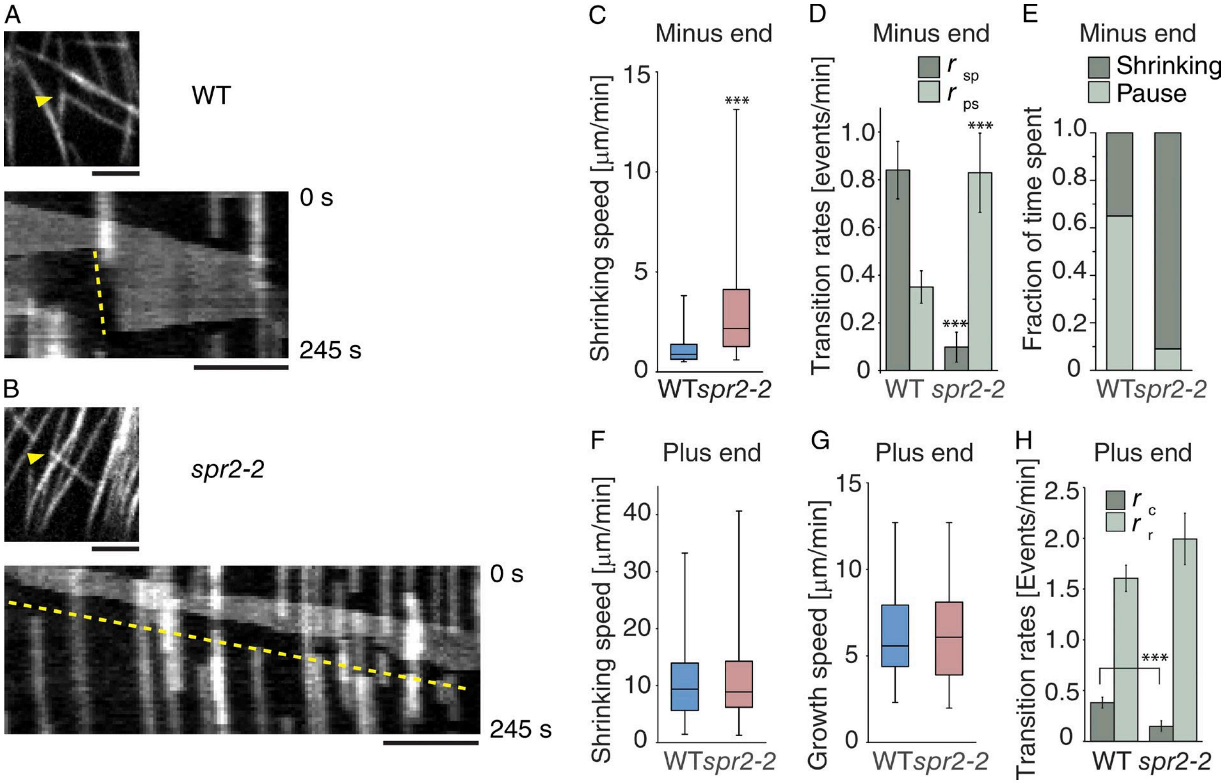

Figure 2. ***spr2-2* mutants show rapid minus-end depolymerization.** **(A and B)** Confocal images (top) and kymographs (bottom) of MTs displaying minus end shrinking in etiolated hypocotyl cells of WT (A) and *spr2-2* mutant (B). Arrowheads indicate minus ends. Dashed lines highlight the position of the minus end in the kymograph. **(C)** Boxplots for minus-end shrinking speed of MTs in WT (*n* = 142 MTs from seven cells) and *spr2-2* (*n* = 154 MTs from six cells). Asterisks indicate a significant difference by Mann–Whitney *U* test (***, P < 0.001). **(D)** Rates of the transition from shrinkage to pause (r_{sp}) and pause to shrinkage (r_{ps}) of MT minus ends. The asterisks indicate a significant difference by rate ratio test (frequency of r_{sp} is *n* = 58 in WT and *n* = 25 in *spr2-2*; ***, P < 0.001, and r_{ps} is *n* = 76 in WT and *n* = 30 in *spr2-2*; ***, P < 0.001). **(E)** Fractions of time spent in dynamic polymer states of the minus end. Total time spent is 256 min from 107 minus ends in WT and 335 min from 154 minus ends in the *spr2-2* mutant. **(F and G)** Boxplots for plus end shrinking and growth speeds, respectively, in WT (*n* = 230 MTs from seven cells) and *spr2-2* mutant cells (*n* = 185 MTs from six cells). **(H)** Catastrophe and rescue rates of MT plus ends. The asterisks indicate a significant difference by rate ratio test (***, P < 0.001). Bars, 3 µm. Errors in bar graphs are SEM. In the boxplots, the box represents the range from the 25th to 75th percentile, the horizontal line marks the median value, and the whiskers span from the 2.5 to 97.5 percentile.

only observed to label plus ends while in a growing state; Fig. S1). The shrinkage velocities of the labeled ends were clustered in a narrow distribution with a relatively slow mean velocity (Fig. 3 C; mean = 0.92 µm/min from 36 severed MTs), whereas the unlabeled ends had a wider range of velocities with a much higher mean (mean = 6.90 µm/min; P < 0.001, Mann–Whitney *U* test). The observed velocity differences between severed ends were consistent with previous observations of end stability in animal cells after laser severing, where minus ends also shrunk more slowly than plus ends (Jiang et al., 2014). Thus, SPR2-GFP appears to be recruited to minus ends generated by laser disruption, and these ends represent a slower class of shrinking ends after severing.

To ask whether SPR2 protects shrinking minus ends generated by laser severing, we repeated this experiment in the *spr2-2* mutant. Because there was no SPR2-GFP to label minus ends, we measured the velocities for all ends created by laser severing. The distributions of shrinking velocities were significantly different between the mutant and WT controls (P < 0.001, Mann–Whitney *U* test), with the class of velocities corresponding to that of the SPR2-GFP–labeled ends in WT cells (mean = 0.86 µm/min from 62 severed MTs) being distinctly missing in the mutant (Fig. 3, B and C). Collectively, these results indicate that SPR2 is able to recognize minus ends created by different processes and protect them from rapid depolymerization.

SPR2 function increases MT catastrophe

SPR2 protein was also observed to accumulate at growing plus ends (Figs. 1 and S1). Compared with its effect on minus ends, loss of SPR2 activity had a more modest effect on plus-end dynamics. Growth and shrinking velocities were not significantly different between WT and mutant (Fig. 2, F and G), nor were the observed rescue rates (Fig. 2 H). However, the catastrophe rate in the mutant was ~40% of that in WT (0.38 min^{-1} vs. 0.15 min^{-1}; P < 0.0001, rate ratio test), suggesting that SPR2 function normally increases the likelihood of plus-end catastrophe. Because polymerization velocities are quantitatively similar between WT and mutant, and because rescue is not significantly different, the reduction in catastrophe suggests that plus ends on average increase in length more rapidly when SPR2 function is lost. The effect of this plus-end stabilization on MT persistence is explored in the modeling studies presented at the end of this results section.

SPR2 function is required for light stimulated cortical array reorientation

To study the role of SPR2 in cortical array organizational dynamics, we investigated its function in the reorganization of cortical arrays in response to light stimulation. As part of the phototrophic response, perception of blue light causes cortical arrays in dark grown hypocotyl cells to undergo a rapid

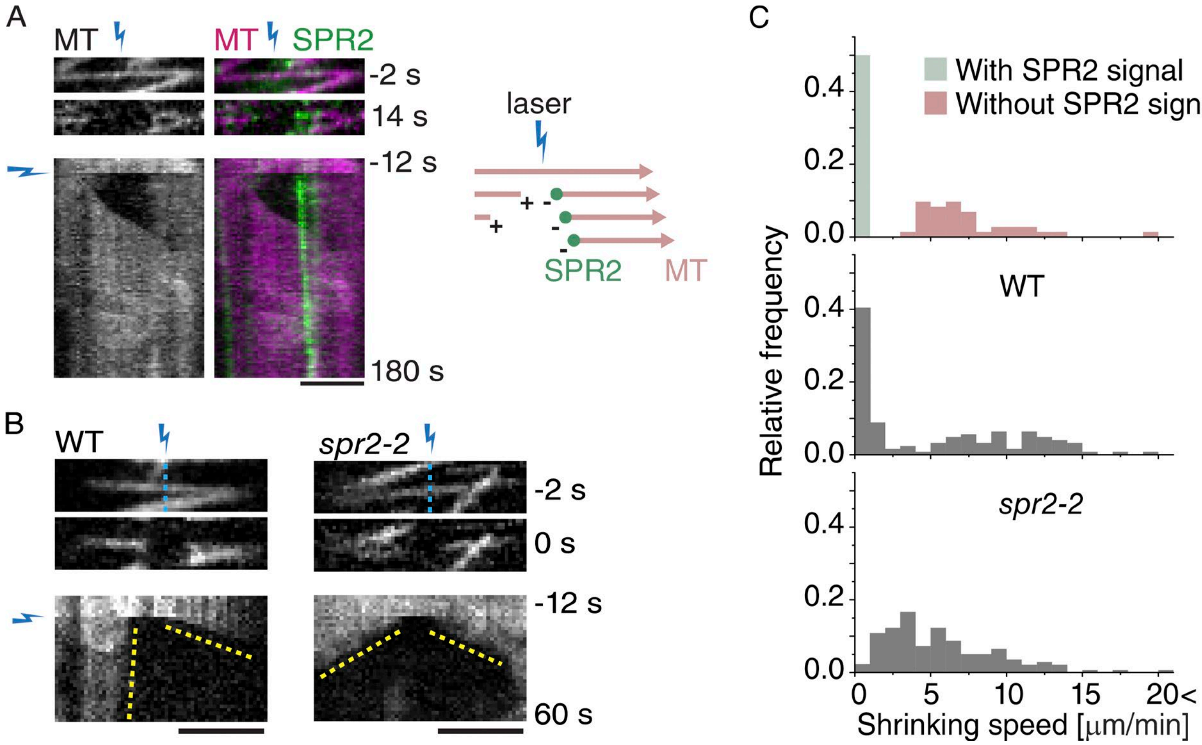

Figure 3. **MT ends after photoablation in vivo. (A)** Representative images of MTs and SPR2 before and after laser ablation. Lightning bolts indicate laser ablation position and time. Kymographs illustrate MT and SPR2 dynamics (Fig. S2). A schema of MT laser ablation is shown on the right. The plus and minus signs indicate the MT plus and minus ends, respectively. **(B)** MT laser ablation in WT and *spr2-2.* Representative images (top) and kymographs (bottom) of MTs before and after laser ablation (blue lightning bolts) in WT and *spr2-2* cells. Yellow dashed lines trace the position of the MT ends in the kymographs. Blue lightning bolts and dotted lines show the times and locations of photoablations. **(C)** Histograms of the relative frequency of MT end shrinking velocities of the MT ends generated by laser ablation. From top to bottom they show the velocities in plants expressing SPR2-GFP and mCherry-TUA5 (*n* = 36), mCherry-TUA5 in WT (*n* = 62), and *spr2-2* (*n* = 69). Note that each ablation generates two shrinking MT ends. The distribution of shrinking speeds after severing are significantly different ($P < 0.01$, Mann–Whitney *U* test).

and dramatic 90-degree shift, from a transverse orientation to the main axis of cell growth to a longitudinal configuration (Fig. 4 A; Laskowski, 1990; Nick et al., 1990; Ueda and Matsuyama, 2000; Lindeboom et al., 2013). A consequence of this reorientation is to redirect trajectories of cellulose synthase complexes in the plasma membrane and thus modify cell wall structure (Paredez et al., 2006). This reorganization is driven by the amplification of a new population of MTs created by katanin-mediated severing at MT crossovers, a process that generates new populations of plus and minus ends in a short period of time and creates ~85% of the new longitudinal MTs (Lindeboom et al., 2013). Our experiments had revealed that SPR2 function acts to affect minus- and plus-end dynamics in vivo, whereas a previous study suggested that SPR2 can act at crossovers to suppress severing (Wightman et al., 2013). We hypothesized that SPR2 might act to promote array reorientation, either by supporting MT amplification through its protection of minus ends or by modulating katanin action at crossovers.

To test whether SPR2 function is required for cortical array reorientation in response to blue light, we measured the rate of cortical array reorientation in etiolated hypocotyl cells of the *spr2-2* mutant expressing mCherry-TUA5 to visualize MTs (Fig. 4, A and B; and Video 6). We observed that reorientation speeds were significantly slower in the *spr2-2* mutant than in WT ($P = 0.0192$, Mann–Whitney *U* test; Fig. 4 C). These results indicated that SPR2 function is required for efficient array reorientation in response to blue light. Consistent with previous observations (Yao et al., 2008), at the onset of the light stimulus, the pitch of transverse cortical arrays in *spr2-2* cells was slightly shifted toward the left (2 degrees in 17 WT cells and 170 degrees in 17 *spr2-2* cells; $P < 0.05$, Watson's U^2 test, $U^2 = 0.2321$, critical value 0.187; Fig. 4, A and B).

SPR2 supports rapid array reorientation by promoting severing opportunity time

To ask whether SPR2 function in reorientation is related to the crossover severing mechanism, we compared the frequency of severing after crossover formation in the *spr2-2* mutant to that in WT. After observation of the formation of a crossover, severing was assessed either as formation of an optically resolved gap in the mCherry-TUA5 signal or by the appearance of a new growing end at the crossover site, both of which absolutely require the action of katanin p60 (Lindeboom et al., 2013). In WT cells, evidence for severing was detected at 38.7% of sampled crossover sites created over the course of reorientation (490 out of 1,266 events observed in six cells, six plants; Fig. 5 A). In contrast, in *spr2-2* cells, severing was observed at only 23.7% of crossover sites, a reduction of nearly 40% ($P < 0.001$, binomial test, 251 of 1,056 crossover events observed in six cells in six plants; Fig. 5 A). Thus, SPR2 function significantly increases the likelihood that severing occurs once a crossover is created.

How does SPR2 act to promote severing likelihood at crossovers? One possibility is that SPR2 promotes katanin activity at crossovers, a function consistent with the observed elevation of SPR2-GFP signal at crossovers (Wightman et al., 2013; this study). We thus first determined whether the prominent

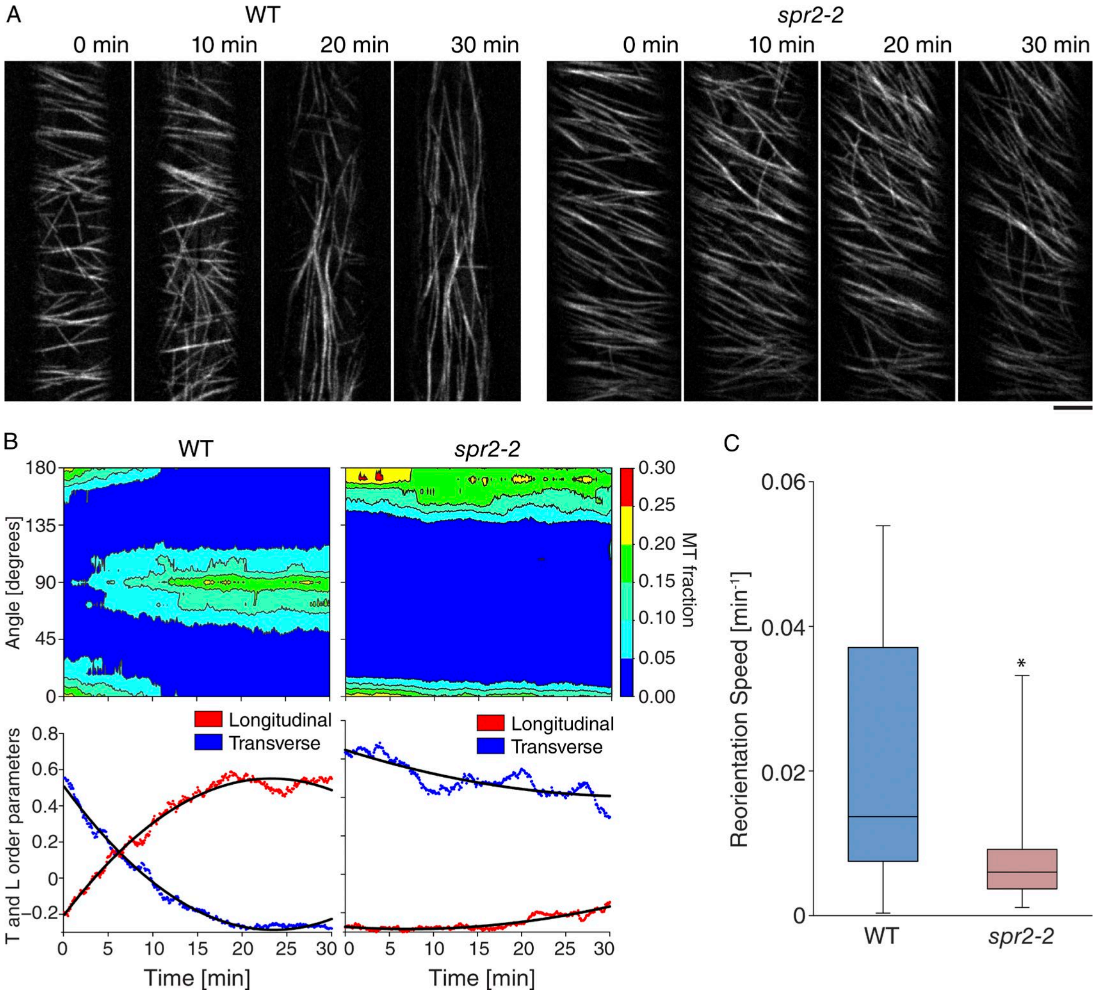

Figure 4. **SPR2 activity is required for efficient MT reorientation. (A)** MT reorientation in WT and *spr2-2* etiolated hypocotyl cells, as visualized by expression of mCherry-TUA5. Bar, 5 µm. See also Video 6. **(B)** Distributions of MT angles over time (Materials and methods) shown in contour plots (top) and transverse (T) and longitudinal (L) order parameters over time with a quadratic fit (black lines, bottom) for the cells shown in A. **(C)** Boxplots for reorientation speed (min^{-1}) comparing WT (17 cells) and *spr2-2* (17 cells). The asterisk indicates a significant difference by Mann–Whitney *U* test (*, P = 0.0192). In the boxplots, the box represents the range from 25th to 75th percentile, the horizontal line marks the median value, and the whiskers span from the 2.5 to 97.5 percentile.

SPR2-GFP signal at crossovers was indeed evidence of protein accumulation or whether the higher signal might be due simply to a superimposition of two MT lattices and consequently their associated proteins. We analyzed 547 crossovers in six plants expressing mCherry-TUA5 and SPR2-GFP (Fig. 5 C; Materials and methods) and measured, after local background subtraction, the ratio of SPR2-GFP signal to mCherry-TUA5 signal over the course of crossover formation. If the SPR2-GFP signal increase is caused by simple superimposition, then this ratio should remain constant. However, the signal ratio was observed to rise significantly, indicating that SPR2-GFP in fact accumulates at crossovers, suggesting an increased crossover affinity for SPR2.

To test whether katanin action itself is affected by SPR2, we measured the distribution of time intervals from the time of crossover formation, which is when a new site for katanin recruitment is created, to the time when severing is observed. The prediction is that this distribution should on average show longer sever waiting times when katanin recruitment and/or activity is impaired. However, the waiting time distributions were not significantly different in our sample sizes, with means of 43.7 versus 46.7 s for WT versus the *spr2-2* mutant, respectively (P = 0.086, Mann–Whitney *U* test, $n = 490$ and 251 events, respectively; Fig. 5 B). Thus, we did not find any evidence for either stimulation or repression of katanin activity by SPR2 function during light-stimulated cortical array reorientation.

If severing activity is not reduced in the *spr2-2* mutant, then what explains the significant reduction in severing likelihood after crossover formation? In time-lapse image series, it is apparent that the increased rate of loss at the minus ends of MTs results in a population of shorter and rapidly treadmilling MTs (Video 7). We reasoned that rapidly treadmilling polymers might be expected to erase crossovers more quickly on average than more slowly treadmilling polymers, leaving less opportunity for severing to occur and thus reducing the likelihood of severing. Measuring the true severing opportunity times in vivo is challenging, because severing of either MT causes destruction of the crossover and thus truncates the distribution of these intrinsic waiting time values for the remaining MT. However, there are two testable predictions for the crossover events that are resolved by depolymerization from either the plus or minus end, as opposed to those resolved by severing. First, the expected lifetime of such crossovers should be shorter in the *spr2-2* loss-

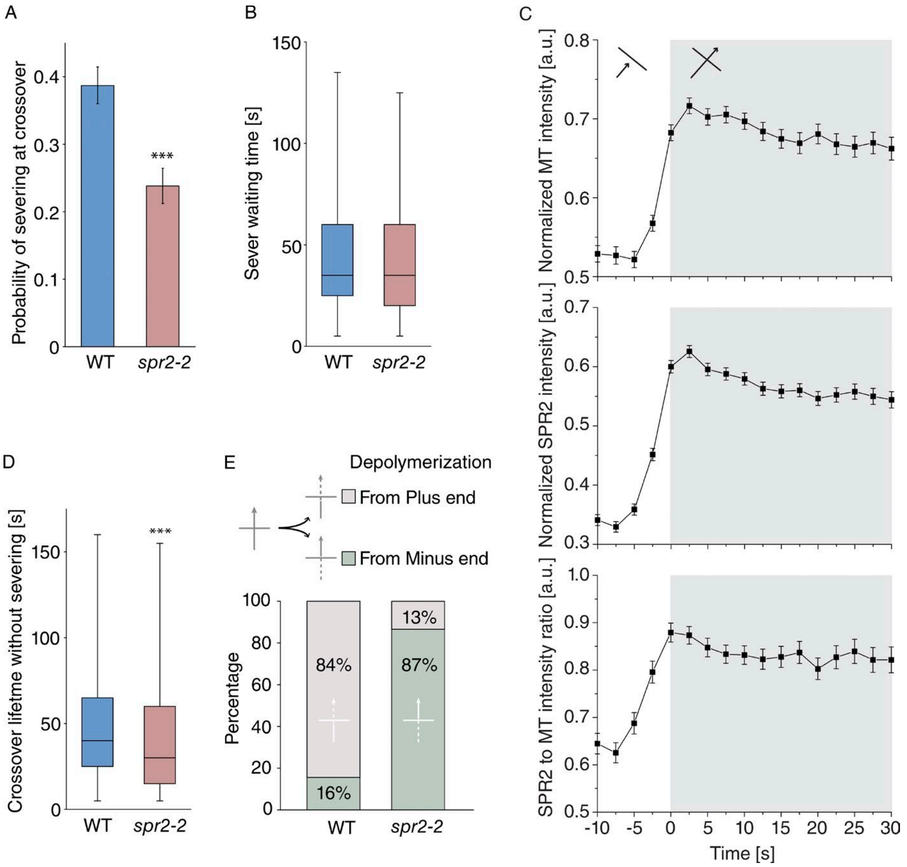

Figure 5. **Rapid minus-end depolymerization causes lower severing probability at crossovers in the *spr2-2* mutant. (A)** Observed probabilities of MT severing events per crossover in WT (*n* = 1,266 events in six cells) and *spr2-2* plants (*n* = 1,056 in six cells). The asterisks indicate a significant difference by Fisher's exact test (***, P < 0.001). **(B)** Boxplots for lifetime of MT crossovers with severing (*n* = 484 from WT and *n* = 251 from *spr2-2*; no significant difference by Mann–Whitney *U* test). **(C)** MT and SPR2 signal intensities at crossovers. Top: Relative mCherry-TUA5 intensity during crossover formation. Middle: Relative SPR2-GFP intensity during crossover formation. Bottom: SPR2-GFP to mCherry-TUA5 signal intensity ratio during crossover formation. Gray background indicates the time where the crossover is present (*n* = 547 crossovers in six cells). **(D)** Boxplots for lifetime of MT crossover without severing (*n* = 782 from WT and *n* = 810 from *spr2-2*). The asterisks indicate a significant difference by Mann-Whitney *U* test (***, P < 0.001). **(E)** Fraction of crossovers resolved, classified as caused by either plus-end or minus-end depolymerization in WT (*n* = 782 crossovers in six cells) and *spr2-2* plants (*n* = 810 crossovers in six cells). In the boxplots, the box represents the range from 25th to 75th percentile, the horizontal line marks the median value and the whiskers span from the 2.5 to 97.5 percentile. The error bars in A represent the 95% confience interval (CI), and the error bars in C represent the SEM.

of-function mutant, and second, this class of crossover should be resolved more frequently by minus-end depolymerization in the mutant. Indeed, the mean lifetime of crossovers resolved by depolymerization was observed to be significantly reduced in the *spr2-2* mutant (43.9 s) compared with WT (50.6 s; P < 0.001, Mann–Whitney *U* test; Fig. 5 D), and the frequency by which crossovers were resolved by minus loss was not only higher in the mutant but also dominant, with 83.8% of non-severed crossovers being resolved by minus-end loss (679 of 810 events) as compared with 11.4% in WT (89 of 782 events; P < 0.001, Fisher's exact test; Fig. 5 E). These results support the hypothesis that SPR2 function increases severing likelihood at crossovers by reducing the severing opportunity time.

Simulations of MT amplification propensity

Although our experimental measurements suggested that SPR2 stabilization of minus-end dynamics facilitates the severing-driven MT amplification mechanism, SPR2 loss of function affects not only minus-end dynamics but also plus-end dynamics (Fig. 2). To aid further exploration of the role SPR2 plays in MT severing and amplification and to probe the relative contributions of dynamics at both MT ends, we built quantitative models and performed simulations of MT amplification (Fig. 6 A). Our models describe the fate of a single longitudinal MT impinging on a nondynamic transverse array of MTs or MT bundles. The MT dynamical parameters, as well as the spacing of the opposing array, are set to the experimental values measured in WT or *spr2-2* mutant cells (Table S1; Materials and methods). In keeping with our observation that the activity of katanin is not significantly dependent on SPR2 in the cells under study, we implemented a unimodal intrinsic waiting time distribution for severing to occur at any newly created crossover based on optimization to match observed sever waiting time distributions (Materials and methods). Sampling from this distribution then yields a potential sever waiting time. Whether or not this severing event is actually realized depends on whether the crossover is still present (i.e., has not been erased by shrinkage of either the minus or the plus end of the crossing MT). When an MT is severed, the newly created plus end is rescued with the measured frequency and otherwise shrinks. During a single run of the simulation, we track the number of MTs as a function of time. Two distinct outcomes are possible: (1) the initial MT and any progeny it creates through severing all disappear after a finite time (extinction), or (2) the number of MTs grows exponentially in time (amplification). By generating a large number of independent simulations of this stochastic process, we can characterize the propensity of amplification, which is a function of both the extinction probability and the amplification rate.

These simulations revealed that the *spr2-2* mutant is predicted to have a markedly lower extinction probability than WT (Fig. 6 B), suggesting that if all other things are equal, then it should be a stronger amplifier. The lower extinction probability is caused by the fact that the measured plus-end dynamics of the *spr2*-2 mutant indicate that it is deeper into the so-called unbounded growth regimen (Dogterom and Leibler, 1993) than is WT, conferring an a priori enhanced survival rate even in the presence of severing. Strikingly, however, the amplification of MTs actually lags significantly behind WT (Fig. 6 C). This apparent discrepancy is fully explained by the altered minus-end dynamics in the *spr2-2* mutant. In the mutant, about half as many crossovers are actually severed compared with WT (Table 1). The cause is the much larger fraction

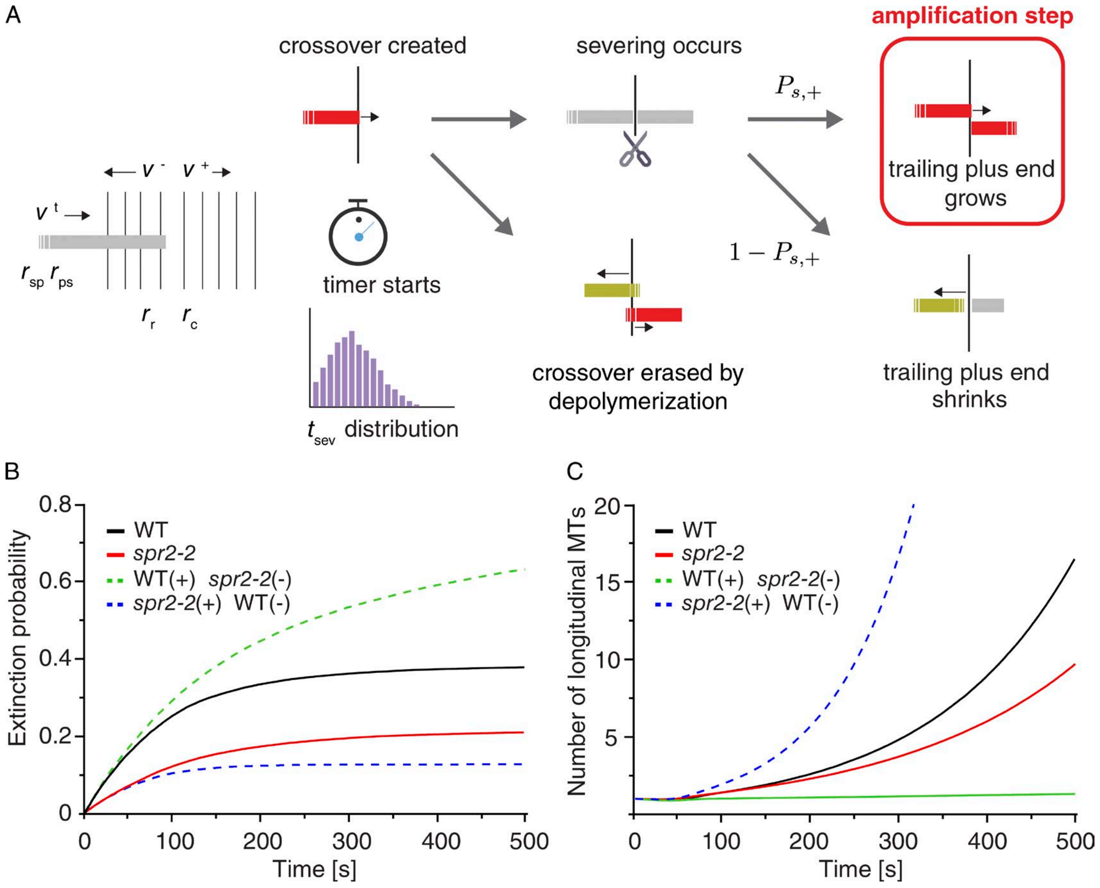

Figure 6. **Simulation of MT amplification by severing in WT and *spr2-2*. (A)** Schematic of the model and flow diagram of the relevant events. After crossover creation, the processes of crossover erasure by MT shrinking and severing compete. When severing occurs, the newly created plus end will be immediately rescued and grow with probability $P_{s,+}$, the primary amplification event. **(B)** Time evolution of the fraction of extinction events in WT and *spr2-2* as well as the two synthetic mutants, WT(+) *spr2-2*(−) and *spr2-2*(+) WT(−). Extinction is more likely in WT than *spr2-2,* because it is less deep into the unbounded growth regimen. For this reason, *spr2-2*(+) WT(−) is the least likely to go extinct, coupling a slowly shrinking minus end (less crossover erasure, and hence more amplification) to strongly unbounded plus-end growth (large intrinsic survival probability). **(C)** Time evolution of the total mean number of MTs starting from a single seed MT (includes the extinction events), showing the stronger amplification of WT compared with *spr2-2.* Note that the synthetic mutant *spr2-2*(+) WT(−) outperforms all others because of its low extinction rate coupled to persistent growth.

of crossovers that are erased by end shrinking, with the large majority being caused by the much-increased minus shrinking (Table 1). These in silico results very closely paralleled those we observed in vivo (Fig. 5 E and Table 1). To further isolate the role of minus-end dynamics on MT amplification, we considered in silico mutants where we permuted the dynamics of the WT and *spr2-2* plus and minus ends. When the *spr2-2* plus end was coupled to a WT minus end, the extinction probability was lower and the degree of amplification higher than in a fully WT system (Table 1). However, when the *spr2-2* minus end was combined with a WT plus end, the extinction probability was large and amplification was almost nonexistent, illustrating the dramatic impact of the strongly enhanced minus-end shrinking on the ability to promote amplification through severing. Collectively, our experimental and modeling results suggest that SPR2 function supports severing likelihood at crossovers and the array reorientation that is driven by severing at crossovers (Lindeboom et al., 2013), likely by promoting the opportunity for severing through its stabilization of MT minus ends. It is possible that SPR2 serves other functions in supporting severing likelihood at crossovers, but experimental measurements of sever waiting time did not support a strong role in regulating katanin activity, and modeling analysis indicated that SPR2-dependent plus-end dynamics act antagonistically to creating a new population of MTs through severing at crossovers.

Discussion

In centrosomal arrays, where MT minus ends are protected by nucleation complexes, array organization is considered to be determined primarily by the control of MT nucleation and assembly at the plus end (Hyman and Karsenti, 1998; Howard and Hyman, 2003). In contrast, the acentrosomal interphase arrays of higher plant cells feature treadmilling polymers, where many minus ends are free and modulation of assembly at both ends is important for determining the properties of individual polymers and how these polymers behave as an interacting assembly. Many regulators that act on plus-end assembly and function have been characterized in higher plants, but no regulators of free minus ends have been reported. Here, we addressed this missing part of the picture by revealing that the *Arabidopsis* SPR2 protein localizes to and tracks free minus ends, whether created by katanin-mediated severing or artificial disruption, where it acts to protect against subunit loss.

SPR2 is distinct from the CAMSAP/patronin minus-end proteins identified in vertebrate cells. CAMSAP2 associates with MTs marked by detyrosination of α-tubulin, a posttranslational modification that marks long-lived MTs (Jiang et al., 2014). Depletion of CAMSAP2 abolishes this population of modified MTs, likely by loss of MT minus-end stabilization (Jiang et al., 2014). SPR2 is not related in sequence to CAM SAP/patronin, and searches of current genome databases indicate that it is unique to the plant lineage. SPR2 also differs from CAMSAP/patronin in its ability to dynamically track depolymerizing minus ends. This property is intriguing and, together with the observation that the rate of depolymerization is markedly higher over extended runs in its absence, indicates that SPR2 action does not simply determine whether the minus end is stable or dynamic and that it can dynamically modulate the rate of subunit loss during depolymerization.

When created by laser severing in vitro, the minus ends of severed MTs appear stable, whereas the plus ends rapidly shorten (Walker et al., 1989). However, in vivo, free minus ends are often observed to show dynamic instability, indicating the presence of in vivo destabilizing factors. In animal cells, katanin p60 has been implicated as a minus-end destabilizing factor in *Drosophila melanogaster* S2 cells (Jiang et al., 2014), as has kinesin 13 in human cell lines (Goodwin and Vale, 2010). In both cases, these actions appear to be antagonized by CAM SAP/patronin to determine minus-end dynamics. Minus-end destabilizing factors have not yet been investigated in plants, but because katanin p60 and kinesin 13 are conserved, they are promising candidates for investigation as possible targets and/or antagonists of SPR2 in controlling plant minus-end dynamics.

A previous study of SPR2 function in *Arabidopsis*, conducted in epidermal cells of petioles and leaves, concluded that SPR2 acts to protect MT crossovers against severing (Wightman et al., 2013). In contrast, in epidermal cells of the etiolated hypocotyl, we did not observe evidence for either a protective or promoting effect of SPR2 on severing at crossovers. It is possible that severing at crossovers is regulated differently among these cell types such that SPR2 has a pronounced effect on severing in leaf cells, but not in cells of the rapidly elongating plant axis. However, there is also a question regarding how severing was measured in the Wightman et al. (2013) study. In that study, severing was measured as the number of severing events per unit area and time. Because severing at crossovers first requires the formation of a crossover, the density of severing events depends on many factors other than severing activity, including MT dynamics, density, organization, and even the action of severing itself as it resolves crossovers. It is therefore challenging to isolate effects on severing activity when measuring changes in the density of crossover severing. It will be interesting to revisit the function of SPR2 in multiple cell types using measures that are specific to individual crossovers, such as severing likelihood and waiting time, and by measuring and taking into account MT dynamics.

That cells might sever existing MTs to generate seeds to create a new population of MTs was proposed as a possible mechanism to explain the rapid buildout of MT arrays in meiocytes and neuronal axons (Roll-Mecak and Vale, 2006). Direct evidence of this proposed mechanism, which is challenging to obtain in the dense arrays of these cells, was made possible by quantitative analysis of individual severing events in interphase plant cells responding to light signals (Lindeboom et al., 2013; this study). Creation of new MT arrays via severing rapidly generates many new minus ends, and the dynamic behavior of these new ends is critical for severing to act as a generative mechanism. Here, we identify SPR2 as a minus end tracking and stabilizing protein that acts to support generation of a new MT array via a severing driven mechanism. Both our experimental and modeling results indicate that an important result of minus end stabilization is to provide a greater opportunity time for severing to act on treadmilling MTs to facilitate creation of a new population of MTs. It remains to be determined whether minus-end factors play a similar role in supporting array creation by severing in animal cells and whether new minus-end factors have yet to be discovered.

Materials and methods

Plant materials and growth conditions

The *spr2-2* and *ktn1-2* mutants and the construction of P_{spr2}-SPR2-GFP were described previously (Shoji et al., 2004; Yao et al., 2008; Nakamura et al., 2010). *spr2-2* and P_{spr2}-SPR2-GFP transgenic lines (*Arabidopsis* Col0 background) were crossed with Col0/35S-mCherry-TUA5– and/or YFP-TUA5–expressing lines (Shaw et al., 2003; Gutierrez et al., 2009). Live-cell imaging experiments were performed in 3-d-old dark-grown etiolated hypocotyls or 4-d-old light-grown cotyledons. Seeds were surface sterilized, stratified for 2 d at 4°C, and sown on 1.5% agar containing 0.5× Murashige and Skoog media with 1% (wt/vol) sucrose at pH 5.7. For dark-grown plants, these plates were exposed to ambient light for 1 h on a benchtop, wrapped in foil to exclude light, and incubated in a near-vertical position at 22°C for 60 to 72 h. Cells in the rapidly elongating zone of 3-d-old etiolated hypocotyls were imaged. T. Hashimoto (Nara Institute of Science and Technology Graduate School of Biological Sciences, Nara, Japan) provided PSR2 and spr2-2 seeds.

Microscopy and image acquisition

All confocal imaging, except for the laser ablation experiments, was performed with a spinning-disk confocal head (QLC100; Yokogawa) mounted on a DMA6000B microscope (Leica) equipped with Adaptive Focus Control (Leica), using a 100× Plan-Apo 1.4 NA oil-immersion objective. GFP was excited at 488 nm (Coherent Cube laser) and

Table 1. **Crossover resolution in WT and *spr2-2***

	Experiments		Simulations			
Parameter set	WT	*spr2-2*	WT	*spr2-2*	WT(+), *spr2-2*(–)	*spr2-2*(+), WT(–)
Number of crossovers analyzed	1266	1056	3.4×10^6	1.8×10^6	0.5×10^6	19.2×10^6
Sever fraction	0.39	0.24	0.61	0.31	0.31	0.68
Depolymerization fraction	0.61	0.76	0.39	0.69	0.69	0.32
Plus-end depolymerization fraction	0.89	0.16	0.92	0.19	0.3	0.87
Minus-end depolymerization fraction	0.11	0.84	0.08	0.81	0.7	0.13

mCherry at 561 nm (Coherent Sapphire laser) using a 405/488/561-nm dichroic beam splitter (Semrock) and an FF01525/50 or an FF01605/64 bandpass emission filter (Semrock), respectively. Images were acquired with an Andor iXon3 EMCCD camera at an EM gain of 300, controlled by Slidebook software (Intelligent Imaging Innovations). The laser ablation imaging was performed with the spinning disk confocal system described previously (Lindeboom et al., 2013), equipped with a 532-pulsed laser (Team Photonics SNG-03E) driven by the iLas system (Roper Scientific).

The time series used for comparing MT dynamics, reorientation dynamics, and crossover outcomes were acquired by exciting mCherry-TUA5 with 300-nm exposures of 561-nm excitation (5 mW as measured at the input fiber of the confocal head) at 5-s intervals over 30 min. We supplemented the seedling with 800 ms of 5-mW 488 laser light with the same 5-s interval to trigger the blue light–induced MT reorientation (Lindeboom et al., 2013). Time-lapse imaging for the SPR2-GFP and mCherry-TUA5 dual-labeled plants was performed at 2.5-s time intervals with 300-ms exposures of 488-nm laser at 5 mW, and 300-ms exposures of 561-nm laser at 5 mW.

The time-lapse imaging for the laser ablation experiments was performed at 2-s time intervals. The WT and *spr2-2* seedlings expressing YFP-TUA5 were excited by a 491-nm laser at 8.5 mW (measured at the optical fiber as it enters the spinning disk head) for 300-ms exposure time. The SPR2-GFP and mCherry-TUA5 dual-labeled plants were imaged with 500-ms exposures of 491-nm excitation at 8.5 mW and 300-ms 561-nm excitation at 8.5 mW.

Data analysis

To measure MT dynamics, we made kymographs of single MTs in WT and *spr2-2* plants expressing mCherry-TUA5. We used time-phased image subtraction to help identify single dynamic MT ends, as described previously (Lindeboom et al., 2013). Plus and minus ends have distinct dynamic behaviors in *Arabidopsis* cortical arrays (Shaw et al., 2003), with plus ends showing dynamic instability characterized by episodes of rapid growth and shrinking, and minus ends showing pause and slow loss. For all the MTs used to derive end dynamics, we observed both MT ends. In all cases, there was always one and only one end that showed growth for at least five frames. Together, these sets of criteria were used to assign identity to plus and minus ends for analysis of dynamics. To facilitate analysis of MT dynamics, we created kymographs from our time-lapse videos. Kymographs were created by tracing individual MTs using MIJI (Sage et al., 2012), which serves as a bridge between FIJI and MATLAB (MathWorks). The traces of individual MTs were stored in a MATLAB structure, and we used the MATLAB function improfile to generate the kymographs. Polymerization velocities were determined from the slopes of the positions of MT ends in the kymographs, and transition rates were determined by counting the number of peaks (catastrophe) or valleys (rescues) and dividing by the total time of growing plus any pause (catastrophe) or shrinking (rescue).

For the quantification of SPR2-GFP signal, we used image time series acquired from plants expressing mCherry-TUA5 and SPR2-GFP. Image registration was performed based on the mCherry-TUA5 channel with StackReg in ImageJ as described earlier (Lindeboom et al., 2013). We applied an exponential bleaching correction in ImageJ (based on the SPR2-GFP in the entire image frame), followed by rolling ball background subtraction and normalization of the signal intensities. To avoid observer bias based on the distribution of SPR2-GFP signal, we identified branching MT nucleation events by examining only the mCherry-TUA5 channel and prepared kymographs of the newly nucleated MT. Observation of nucleation allowed for robust identification of plus and minus ends. On each nucleation kymograph showing only the MT signal, we selected locations of MT lattice, free minus ends, crossovers, and growing MT plus ends. We then measured the mean signal intensity in each channel in a 3-pixel range around the selected coordinates along the length of the kymograph line and calculated the relative SPR2 signal as SPR2 signal divided by the sum of SPR2 signal and MT signal.

We used the same kymographs of newly nucleated MTs as described in the previous paragraph to study SPR2 signal intensity accumulation at the MT minus end. In each kymograph of the MT signal only, we identified a location where a free minus end was observed to be separated from the mother MT by an optically resolved gap (Nakamura et al., 2010). We aligned the signals for multiple minus ends by the location of the edge of the MT signal at the minus end as identified by eye, thus defining the “zero” pixel position. A measurement region was defined extending from 5 pixels before the zero position to 7 pixels past this location in to the MT lattice. For both the SPR2 and MT signal, we normalized the signal over this region by first subtracting the minimum intensity value from all pixels and then dividing the intensity by the maximum of the remaining values, resulting in an intensity range for both the SPR2 and MT signal between 0 and 1 in the measurement region for each observed minus end. To evaluate the distributions of the MT and SPR2 signal intensities, these normalized values were averaged by pixel position over the population of measured regions. To assess SPR2 enrichment at the minus end in individual observations, the sum of SPR2 signal in a 3-pixel subregion centered at the tip was compared with the sum from an adjacent 3-pixel subregion internal to the tip.

The quantification of MT orientation and ordering were performed as described previously (Lindeboom et al., 2013) using the ImageJ plugin LOCO to assign a local orientation value to each pixel over a threshold value of intensity and processing these data in MATLAB to measure angular distributions and calculate order parameters over time.

To calculate the distribution of distances between transverse MTs in images of cortical arrays at the initiation of light stimulation, we rotated the first image of each time series so that the long axis of the cell is on the vertical axis. We applied a rolling-ball background subtraction with a radius of 30 pixels in ImageJ and selected the vertical midline of the image. We extracted the signal intensity peaks in the data with the MATLAB function findpeaks and used the normalized first derivative of the peak prominence as a selective filter to identify those associated with MT signal. We determined that for our data, values above 0.015 were reliably associated with MT signal, whereas lesser values represented background. We calculated the inter-MT distances using the positions of the detected MT signal peaks. Fig. S3 shows an example for an *spr2-2* cell with an overlay of the detected peaks in cyan on the fluorescence image used as input data.

For the analyses of crossover creation and resolution, we marked the x and y coordinates for every observed crossover in the region of interest (Video 8), the start and end times (the time of crossover creation and the time of resolution by either depolymerization or severing), the angles of the “old” and “new” MTs, and whether the old and/or new MT at the crossover got severed. In case of no severing, we marked whether the crossover was resolved by plus end or minus-end depolymerization. If a severing event took place at the crossover, we documented whether the lagging MT was initially growing or shrinking.

This crossover analysis was also performed in conjunction with the evaluation of SPR2 and MT signal intensity at the crossovers. We first registered the images using a modified version of StackReg (Thévenaz et al., 1998) to register the MT channel of each time series and then apply the transformation matrix to the SPR2 channel. Photobleaching correction was performed using an exponential fit to the mean signal intensities for each channel. We then defined a 7-by-7-pixel array centered around each of the identified crossover positions. The 1-pixel-wide outer border was used for estimating the local background signal intensities for each channel. To make these estimations, we first discarded the highest 12 (out of 24) border pixel values in each frame, as they typically represented the signal of the two MTs forming the crossover. The median intensity value of the remaining border pixels was then calculated to estimate the local background. To calculate the crossover signal intensity, we subtracted the local background value from each of the pixels in the inner 5 × 5 pixels of the crossover region of interest and summed to obtain the total crossover intensity. Finally, we normalized the summed signal intensity of the inner 5-by-5-pixel region by dividing the total intensity by the maximum region of interest intensity for the duration of the crossover for each individual crossover. The normalized crossover intensities were calculated for both the SPR2 and MT signals, and the crossover event intensities were aligned with each other based on the start frame of the crossover event. We calculated the SPR2 to MT signal ratio by dividing the normalized SPR2 intensity by the normalized MT intensity. The standard errors for mean ratios at each time point were calculated from the error propagation of the standard errors of the separate SPR2 and MT signal intensities.

Stochastic model

We set up a stochastic model to elucidate the impact of MT minus-end dynamics on the reorientation mechanism. We focus on the initial stage of the process, which we take to be up to 500 s after the first exposure to light. In this stage, the initial transverse array can be considered as a constant background. We model it as a lattice of perfectly parallel filaments, with the distance d between neighboring filaments distributed according to an exponential distribution with a short length cutoff

$$f(d) = \begin{cases} 0, & \text{if}\, d \leq 0.5\ \mu\text{m} \\ \frac{1}{D} e^{-\frac{d}{D}}, & \text{if}\, d > 0.5\ \mu\text{m}' \end{cases}$$

with D chosen such that the mean spacing between neighboring filaments d_{avg} is consistent with the experimentally measured one (Tables 1 and S1).

The model tracks the fate of a single longitudinal MT undergoing dynamic instability both at its plus and minus end as it traverses the transverse lattice. This longitudinal MT is modeled as a straight line nucleated with the plus end in the growing state, with growth velocity v^+, and the minus end in the paused state. The growth of the MT plus end can be interrupted by a catastrophe, modeled as a Poisson event with rate r_c. The plus end then shrinks with shrinking velocity v^- and either disappears or undergoes a rescue with rate r_r. Given the absence of polymerization at MT minus ends (Fig. 2 E), in our model, the minus end can be either in the paused state or in the shrinking state, with minus-end shrinking velocity w. The rate of transitioning from the paused state to the shrinking state is r_{ps}, and the rate of transitioning from the shrinking to the pausing state is r_{sp}. All the rates and the velocities used in the simulations are in agreement with the mean values of the same quantities measured experimentally (Fig. 2 and Table S1).

When the plus end impinges on a transverse MT, it creates a crossover. This crossover can either be erased caused by the shrinkage of either of the two ends or survives long enough to lead to a severing event (Fig. 6 A). The occurrence (or not) of the severing event is determined in part by an intrinsic severing waiting time distribution $W_{k\theta}(t)$:

$$W_{k\theta}(t) = \frac{t^{k-1}}{\theta^k \Gamma(k)} e^{-\frac{t}{\theta}};$$

i.e., gamma probability density function (Papoulis, 1984), where k and θ are the shape and scale parameters of the distribution, and

$$\Gamma(k) = \int_0^{+\infty} dx\, x^{k-1} e^{-x},$$

the Euler gamma function (Abramowitz and Stegun, 1965). Experimentally, one can only determine the conditional waiting time distribution; i.e., the waiting time given that the crossover has not been erased by either plus or minus end shrinking. We therefore determined the parameters k and θ such that the conditional sever waiting distribution as determined in the simulations, optimally match those observed in the experiments (Fig. S4 and Table S1), making the reasonable assumption that the activity of katanin and, hence, the intrinsic waiting time distribution do not depend on the difference in minus-end dynamics between WT and *spr2-2*. In keeping with our assumption that only longitudinal MTs have significant dynamics in the first 500 s, all severing events affect only longitudinal MTs.

When the severing event happens, the newly created plus end of the lagging MT either grows with probability $P_{s,+}$, or shrinks with probability $1 - P_{s,+}$, according to experimental measurements (Table S1). The newly created minus end at a severing of the leading MT either shrinks with probability $Q_{s,-}$, or pauses with probability $1 - Q_{s,-}$ (Table S1). Given that $Q_{s,-}$ is not directly measurable, we chose this parameter such that the time spent in either of the possible states for the minus end is in agreement with experimental observations.

Our simulations consist of $n = 5 \times 10^4$ trials in which a single longitudinal MT nucleated at a random position in the transverse lattice of transverse and any descendants it creates through severing are tracked over time. Every trial ends either after 500 s and the number of longitudinal MTs still alive is greater than zero (amplification), or whenever the original MT and all of its progeny have shrunk back to zero length as a result of dynamic instability of the two MT ends (extinction). Apart from the fact that at later stages the degradation of the transverse array can no longer be ignored, the choice of limiting the simulation time to 500 s is also motivated by practical computational constraints: the exponential amplification of the number of longitudinal MTs requires an unsustainable exponentially increasing processing time.

Our simulations confirm the experimental observations, and quantitatively show that even though the extinction probability of an MT with its progeny is smaller in the *spr2-2* mutant than in the WT (Fig. 6 B), the exponential amplification of the number of longitudinal MTs in the WT is stronger than in the *spr2-2* case (Fig. 6 C). This confirms that SPR2 acts to increase the probability of severing at crossovers by extending the crossover lifetimes, which would otherwise be strongly reduced because of fast minus end shrinking. The result that extinction of MTs is more likely in WT than in the *spr2-2* mutant, depends on the fact that *spr2-2* mutant is deeper in the so-called unbounded growth regimen (Dogterom and Leibler, 1993); indeed, the deeper an MT is in the unbounded growth regimen, the larger is its probability to live indefinitely (Bicout, 1997). The degree to which the MT is in the unbounded growth regimen is characterized by the value of its mean growth velocity:

$$J = \frac{v^+ r_r - v^- r_c}{r_r + r_c}.$$

The importance of a stable minus end for the overall speed of the reorientation mechanism can be also be confirmed by considering two synthetic mutants created in silico: MTs with WT background but with the *spr2-2* mutant's parameters for the minus end (WT(+) *spr2-2*(−)), and MTs with *spr2-2* mutant background but with WT parameters for the minus end (*spr2-2*(+) WT(−)). Fig. 5 C shows that the (WT(+) *spr2-2*(−) mutant almost completely fails to amplify the number of longitudinal MTs. In contrast, the *spr2-2*(+) WT(−) mutant shows a significantly stronger amplification (one order of magnitude greater than in the normal WT case), once again showing the key importance of a stabilized minus end in promoting the probability of severing at crossovers.

These results are further confirmed by the analysis of the statistics of crossovers (Table 1), where the probability of crossover removal caused by depolymerization depends most strongly on the behavior of the minus end rather than on the behavior of the plus end. Indeed, *spr2-2* and WT(+) *spr2-2*(−) exhibit the same depolymerization probability, and the depolymerization probability of WT and *spr2-2*(+) WT(−) are comparable, albeit slightly different. The same agreement is shown by the probability that given the crossover is erased, the erasure happens through the shrinkage of either of the two ends of the MT (Table 1).

However, even if the model qualitatively explains the underlying mechanism behind the observed amplification of the number of longitudinal MTs, it quantitatively overestimates the number of severing events at crossovers compared with experiments both in WT and *spr2-2* (Table 1). The otherwise good agreement between simulations and experiments for the crossover removal because of depolymerization of either of the two ends suggests that the main reason for this discrepancy rests with our assumption of limiting the dynamics only to longitudinal MTs. Indeed, the model does not account for the possibility of crossover removal because of shrinkage of transverse MTs, as is the case in vivo, as well as the possibility that katanin severs a transverse MT instead of a longitudinal one. This implies that the quantities related to severing events might be affected by these assumptions, whereas quantities that only depend on the intrinsic dynamic instability of MTs, like plus- and minus-end depolymerization, should not be affected by those same assumptions.

Online supplemental material

Fig. S1 shows SPR2-GFP localization on a dynamic MT, highlighting localization to shrinking minus ends and growing plus ends. Fig. S2 displays representative images of SPR2-GFP recruitment to minus ends during an in vivo laser-severing experiment. Fig. S3 presents details about the quantification of MT bundle distributions and results from fitting the sever waiting time distributions are shown in Fig. S4. The model input parameters are listed in Table S1. An overview of SPR2 localization on cortical MTs is presented in Video 1. Videos 2–4 show SPR2 minus-end localization and tracking after a nucleated MT is severed from the nucleation site (Video 2), in a large area overview (Video 3), and after severing at an MT crossover (Video 4). Video 5 provides an example of a laser severing experiment. MT reorientation induced by blue light is compared for WT and the *spr2-2* mutant in Videos 6 and 7; Video 7 includes overlays produced from time-phased subtraction to more easily visualize growth and shrinkage at both polymer ends. Video 8 shows an example of crossovers that detected and were used for analysis of crossovers in WT and *spr2-2* mutant.

Acknowledgments

We thank T. Hashimoto for providing the SPR2-GFP and *spr2-2* seeds, M. Janson and J. de Keijzer for help with instrument setup for the laser ablation experiments, Z. Lansky for advice on image analysis, D. Quint for helpful discussion, and H. Cartwright for assistance with confocal microscopy.

This work was supported by the Carnegie Institution for Science (D.W. Ehrhardt), the National Science Foundation (grant 1158372; D.W. Ehrhardt), and the Human Frontier Science Program (M. Nakamura). The work of M. Saltini is supported by the European Research Council (Synergy grant MODELCELL). The work of B.M. Mulder is part of the research program of the Netherlands Organization for Scientific Research.

The authors declare no competing financial interests.

Author contributions: D.W. Ehrhardt, M. Nakamura, and J.J. Lindeboom designed experimental strategy. M. Nakamura and J.J. Lindeboom carried out experiments. M. Nakamura, J.J. Lindeboom, and D.W. Ehrhardt analyzed data. B.M. Multer and M. Saltini designed and performed the simulations. D.W. Ehrhardt, M. Nakamura, J.J. Lindeboom, and B.M. Mulder wrote the manuscript. M. Saltini edited the manuscript.

Submitted: 18 August 2017
Revised: 1 November 2017
Accepted: 4 December 2017

References

Abramowitz, M., and L.A. Stegun. 1965. Handbook of Mathematical Functions With Formulas, Graphs and Mathematical Tables. Dover Publications, New York. 253.

Akhmanova, A., and M.O. Steinmetz. 2015. Control of microtubule organization and dynamics: two ends in the limelight. *Nat. Rev. Mol. Cell Biol.* 16:711–726. https://doi.org/10.1038/nrm4084

Baskin, T.I. 2005. Anisotropic expansion of the plant cell wall. *Annu. Rev. Cell Dev. Biol.* 21:203–222. https://doi.org/10.1146/annurev.cellbio.20.082503.103053

Bicout, D.J. 1997. Green's functions and first passage time distributions for dynamic instability of microtubules. *Phys. Rev. E Stat. Phys. Plasmas Fluids Relat. Interdiscip. Topics.* 56:6656–6667. https://doi.org/10.1103/PhysRevE.54.5538

Buschmann, H., C.O. Fabri, M. Hauptmann, P. Hutzler, T. Laux, C.W. Lloyd, and A.R. Schäffner. 2004. Helical growth of the Arabidopsis mutant tortifolia1 reveals a plant-specific microtubule-associated protein. *Curr. Biol.* 14:1515–1521. https://doi.org/10.1016/j.cub.2004.08.033

Chan, J., A. Sambade, G. Calder, and C. Lloyd. 2009. Arabidopsis cortical microtubules are initiated along, as well as branching from, existing microtubules. *Plant Cell.* 21:2298–2306. https://doi.org/10.1105/tpc.109.069716

Cyr, R.J. 1994. Microtubules in plant morphogenesis: role of the cortical array. *Annu. Rev. Cell Biol.* 10:153–180. https://doi.org/10.1146/annurev.cb.10.110194.001101

Dogterom, M., and S. Leibler. 1993. Physical aspects of the growth and regulation of microtubule structures. *Phys. Rev. Lett.* 70:1347–1350. https://doi.org/10.1103/PhysRevLett.70.1347

Furutani, I., Y. Watanabe, R. Prieto, M. Masukawa, K. Suzuki, K. Naoi, S. Thitamadee, T. Shikanai, and T. Hashimoto. 2000. The SPIRAL genes are required for directional control of cell elongation in Aarabidopsis thaliana. *Development.* 127:4443–4453.

Goodwin, S.S., and R.D. Vale. 2010. Patronin regulates the microtubule network by protecting microtubule minus ends. *Cell.* 143:263–274. https://doi.org/10.1016/j.cell.2010.09.022

Gutierrez, R., J.J. Lindeboom, A.R. Paredez, A.M.C. Emons, and D.W. Ehrhardt. 2009. Arabidopsis cortical microtubules position cellulose synthase delivery to the plasma membrane and interact with cellulose synthase trafficking compartments. *Nat. Cell Biol.* 11:797–806. https://doi.org/10.1038/ncb1886

Howard, J., and A.A. Hyman. 2003. Dynamics and mechanics of the microtubule plus end. *Nature.* 422:753–758. https://doi.org/10.1038/nature01600

Hyman, A., and E. Karsenti. 1998. The role of nucleation in patterning microtubule networks. *J. Cell Sci.* 111:2077–2083.

Jiang, K., S. Hua, R. Mohan, I. Grigoriev, K.W. Yau, Q. Liu, E.A. Katrukha, A.F.M. Altelaar, A.J.R. Heck, C.C. Hoogenraad, and A. Akhmanova. 2014. Microtubule minus-end stabilization by polymerization-driven CAMSAP deposition. *Dev. Cell.* 28:295–309. https://doi.org/10.1016/j.devcel.2014.01.001

Laskowski, M.J. 1990. Microtubule orientation in pea stem cells: a change in orientation follows the initiation of growth rate decline. *Planta.* 181:44–52. https://doi.org/10.1007/BF00202323

Lindeboom, J.J., M. Nakamura, A. Hibbel, K. Shundyak, R. Gutierrez, T. Ketelaar, A.M.C. Emons, B.M. Mulder, V. Kirik, and D.W. Ehrhardt. 2013. A mechanism for reorientation of cortical microtubule arrays driven by microtubule severing. *Science.* 342:1245533. https://doi.org/10.1126/science.1245533

Magidson, V., J. Loncarek, P. Hergert, C.L. Rieder, and A. Khodjakov. 2007. Laser microsurgery in the GFP era: a cell biologist's perspective. *Methods Cell Biol.* 82:239–266.

Murata, T., S. Sonobe, T.I. Baskin, S. Hyodo, S. Hasezawa, T. Nagata, T. Horio, and M. Hasebe. 2005. Microtubule-dependent microtubule nucleation based on recruitment of gamma-tubulin in higher plants. *Nat. Cell Biol.* 7:961–968. https://doi.org/10.1038/ncb1306

Nakamura, M. 2015. Microtubule nucleating and severing enzymes for modifying microtubule array organization and cell morphogenesis in response to environmental cues. *New Phytol.* 205:1022–1027. https://doi.org/10.1111/nph.12932

Nakamura, M., and T. Hashimoto. 2009. A mutation in the Arabidopsis gamma-tubulin-containing complex causes helical growth and abnormal microtubule branching. *J. Cell Sci.* 122:2208–2217. https://doi.org/10.1242/jcs.044131

Nakamura, M., D.W. Ehrhardt, and T. Hashimoto. 2010. Microtubule and katanin-dependent dynamics of microtubule nucleation complexes in the acentrosomal Arabidopsis cortical array. *Nat. Cell Biol.* 12:1064–1070. https://doi.org/10.1038/ncb2110

Nick, P., R. Bergfeld, E. Schäfer, and P. Schopfer. 1990. Unilateral reorientation of microtubules at the outer epidermal wall during photo- and gravitropic curvature of maize coleoptiles and sunflower hypocotyls. *Planta.* 181:162–168. https://doi.org/10.1007/BF02411533

Oda, Y. 2015. Cortical microtubule rearrangements and cell wall patterning. *Front. Plant Sci.* 6:236. https://doi.org/10.3389/fpls.2015.00236

Papoulis, A. 1984. Probability, Random Variables, and Stochastic Processes. Second edition. McGraw-Hill Inc., New York. 103–104.

Paradez, A., A. Wright, and D.W. Ehrhardt. 2006. Microtubule cortical array organization and plant cell morphogenesis. *Curr. Opin. Plant Biol.* 9:571–578. https://doi.org/10.1016/j.pbi.2006.09.005

Paredez, A.R., C.R. Somerville, and D.W. Ehrhardt. 2006. Visualization of cellulose synthase demonstrates functional association with microtubules. *Science.* 312:1491–1495. https://doi.org/10.1126/science.1126551

Roll-Mecak, A., and R.D. Vale. 2006. Making more microtubules by severing: A common theme of noncentrosomal microtubule arrays? *J. Cell Biol.* 175:849–851. https://doi.org/10.1083/jcb.200611149

Sage, D., D. Prodanov, J.-Y. Tinevez, and J. Schindelin. 2012. MIJ: Making Interoperability Between ImageJ and Matlab Possible. ImageJ User & Developer Conference, Luxembourg.

Shaw, S.L., R. Kamyar, and D.W. Ehrhardt. 2003. Sustained microtubule treadmilling in Arabidopsis cortical arrays. *Science.* 300:1715–1718. https://doi.org/10.1126/science.1083529

Shoji, T., N.N. Narita, K. Hayashi, J. Asada, T. Hamada, S. Sonobe, K. Nakajima, T. Hashimoto, and T. Hashimoto. 2004. Plant-specific microtubule-associated protein SPIRAL2 is required for anisotropic growth in Arabidopsis. *Plant Physiol.* 136:3933–3944. https://doi.org/10.1104/pp.104.051748

Thévenaz, P., U.E. Ruttimann, and M. Unser. 1998. A pyramid approach to subpixel registration based on intensity. *IEEE Trans. Image Process.* 7:27–41. https://doi.org/10.1109/83.650848

Ueda, K., and T. Matsuyama. 2000. Rearrangement of cortical microtubules from transverse to oblique or longitudinal in living cells of transgenicArabidopsis thaliana. *Protoplasma.* 213:28–38. https://doi.org/10.1007/BF01280502

Walker, R.A., S. Inoué, and E.D. Salmon. 1989. Asymmetric behavior of severed microtubule ends after ultraviolet-microbeam irradiation of individual microtubules in vitro. *J. Cell Biol.* 108:931–937. https://doi.org/10.1083/jcb.108.3.931

Wightman, R., G. Chomicki, M. Kumar, P. Carr, and S.R. Turner. 2013. SPIRAL2 determines plant microtubule organization by modulating microtubule severing. *Curr. Biol.* 23:1902–1907. https://doi.org/10.1016/j.cub.2013.07.061

Yao, M., Y. Wakamatsu, T.J. Itoh, T. Shoji, and T. Hashimoto. 2008. Arabidopsis SPIRAL2 promotes uninterrupted microtubule growth by suppressing the pause state of microtubule dynamics. *J. Cell Sci.* 121:2372–2381. https://doi.org/10.1242/jcs.030221

Zhang, Q., E. Fishel, T. Bertroche, and R. Dixit. 2013. Microtubule severing at crossover sites by katanin generates ordered cortical microtubule arrays in Arabidopsis. *Curr. Biol.* 23:2191–2195. https://doi.org/10.1016/j.cub.2013.09.018

Supplemental material

Nakamura et al., https://doi.org/10.1083/jcb.201708130

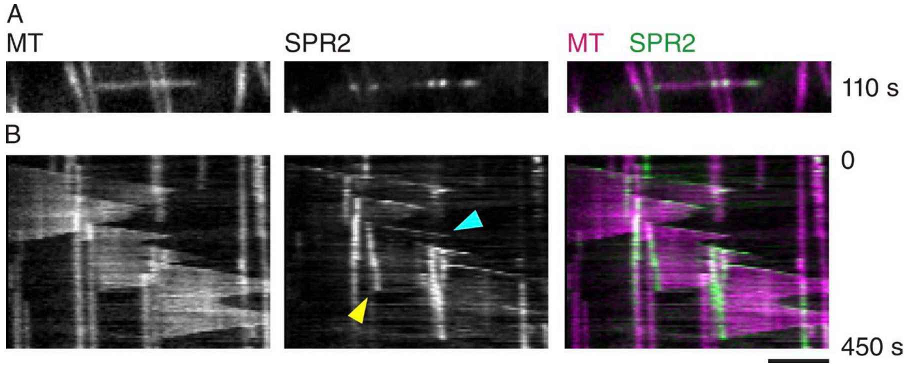

Figure S1. **Dynamic MT labeling of SPR2-GFP on mCherry-TUA5–labeled MTs in 3-d-old dark grown seedlings. (A)** Single image of SPR2-GFP foci on an MT. **(B)** Kymograph of the dynamic colocalization of SPR2-GFP on mCherry-TUA5–labeled MTs. The blue and yellow arrowheads indicate plus and minus end localization of SPR2-GFP, respectively.

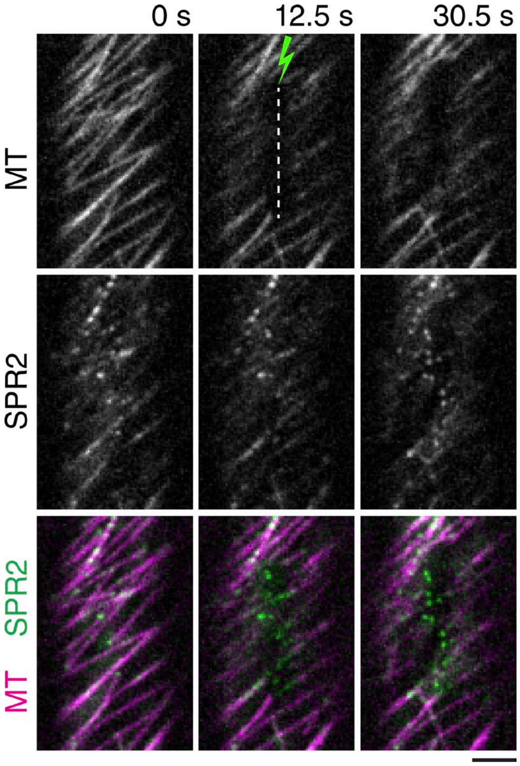

Figure S2. **Representative images of mCherry-TUA5–labeled MTs and SPR2-GFP before and after photoablation.** The green lightning bolt and white dashed line indicate photoablations and the area of photoablation, respectively. Bar, 3 µm.

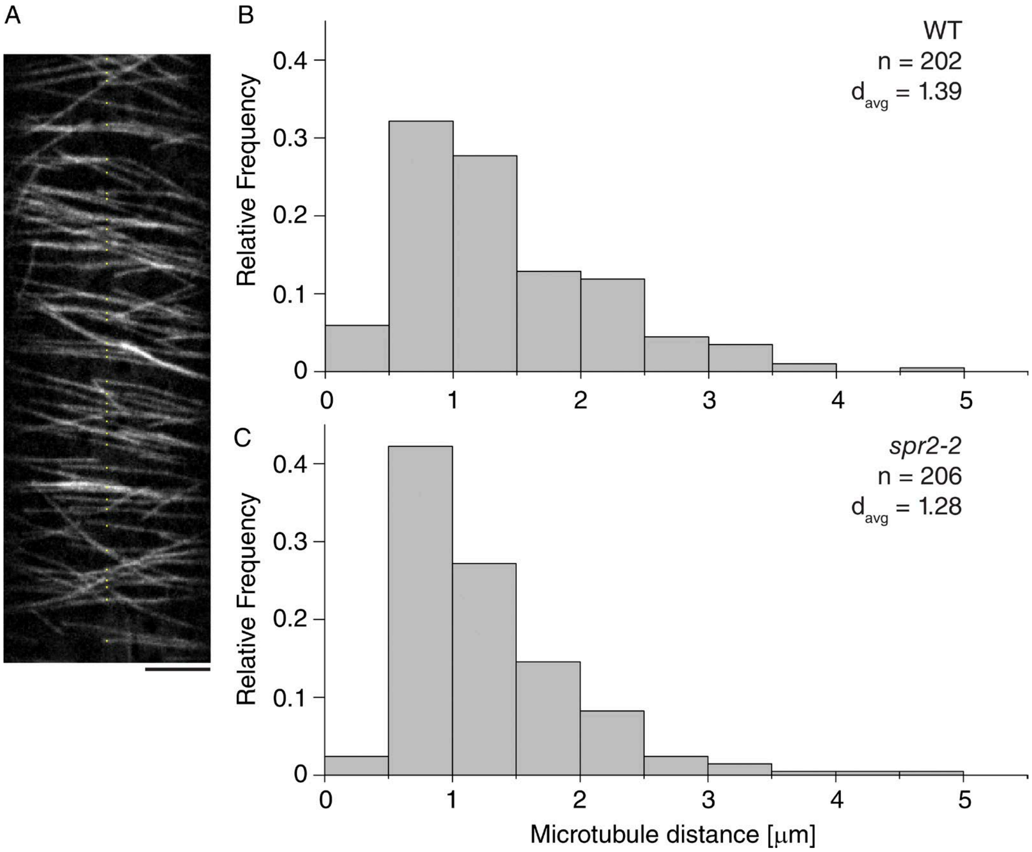

Figure S3. **Transverse MT spacing distribution. (A)** Dark-grown *spr2-2* hypocotyl cell expressing mCherry-TUA5 with detected MTs (Materials and methods) along the vertical midline indicated by dots. Bar, 5 µm. **(B and C)** Distribution of MT distance between longitudinal MTs in WT (B) and *spr2-2* (C).

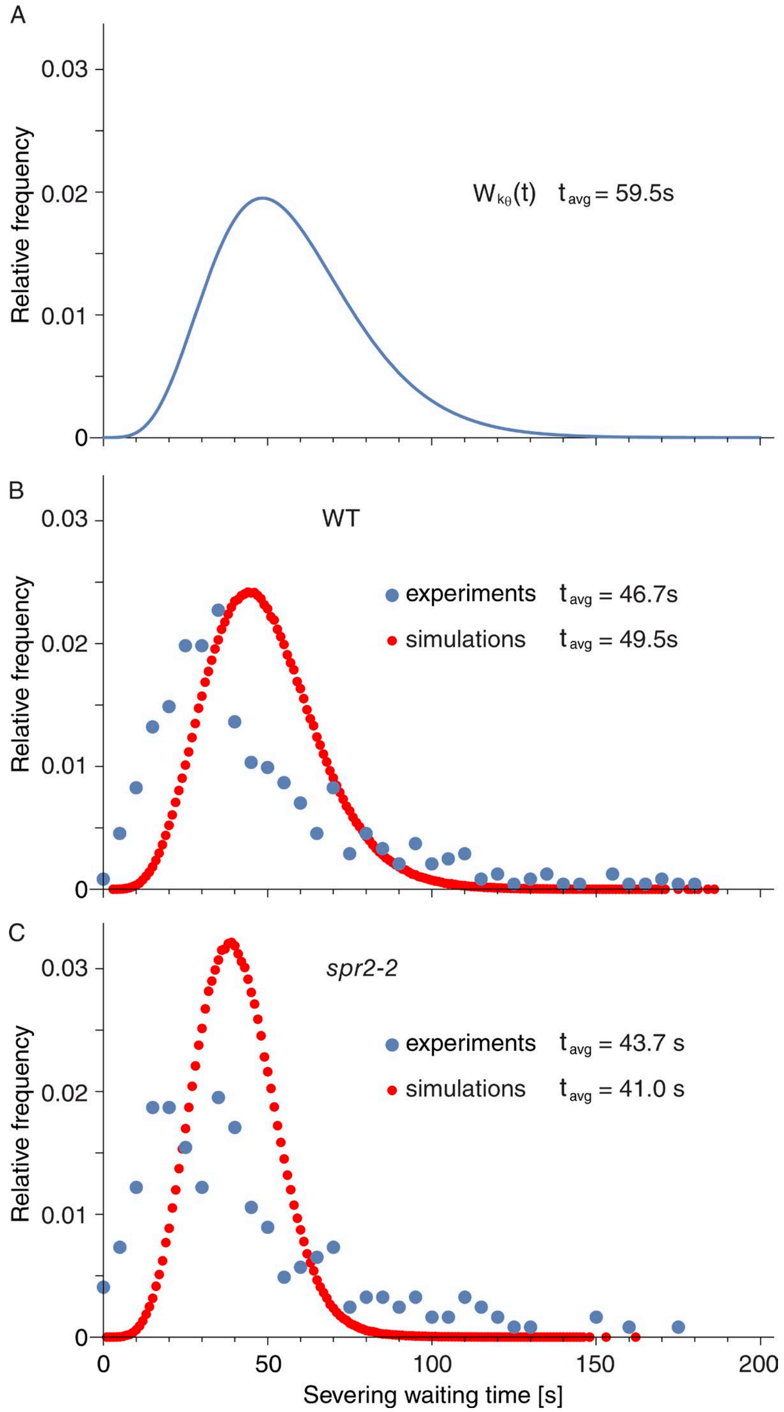

Figure S4. **Intrinsic, conditional, and observed waiting distributions for severing at microtubule crossovers. (A and B)** The optimal intrinsic waiting time distribution (A) and the resultant computed conditional waiting distributions (red dots) compared with the observed distribution (blue dots) in WT cells (B). **(C)** The computed conditional and observed waiting distributions in *spr2-2* cells.

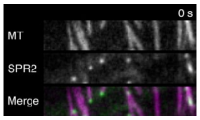

Video 1. **Time series showing dynamic localization of SPR2-GFP– (green) and mCherry-labeled cortical MTs (magenta) in etiolated hypocotyl cells.** Yellow arrowheads and blue arrowheads indicate SPR2 signal tracking minus ends and plus ends, respectively. Images were acquired at 5-s intervals.

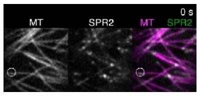

Video 2. **Time series showing dynamic localization of SPR2-GFP– (green) and mCherry-TUA5–labeled cortical MTs (magenta) in etiolated hypocotyl cells.** Dotted circle indicates the site where new MT initiates in a branching manner and is subsequently severed from its initiation site, creating a free minus end. The blue and yellow arrowheads indicate the MT plus end and labeled SPR2 protein tracking the dynamic minus end, respectively. Images were acquired at 5-s intervals.

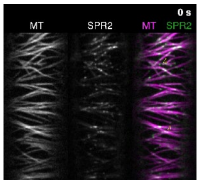

Video 3. **Time series showing dynamic localization of SPR-GFP– (green) and mCherry-labeled cortical MTs (magenta) etiolated hypocotyl cells.** The yellow open arrowheads indicate labeled SPR2 protein tracking the dynamic minus end. Images were acquired at 5-s intervals

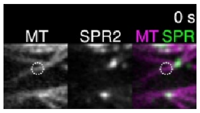

Video 4. **Time series showing dynamic localization of SPR2-GFP– (green) and mCherry-labeled cortical MTs (magenta) in etiolated hypocotyl cells.** Dotted circle indicates a site where an MT crossover is made and the newer MT is severed. The blue arrowhead and yellow arrowheads indicate the newly generated MT plus end and labeled SPR2 protein tracking the new minus end, respectively. Images were acquired at 5-s intervals.

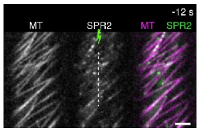

Video 5. **SPR2-GFP decorates MT minus ends generated by photoablation.** Time series showing dynamic localization of SPR2-GFP– (green) and mCherry-TUA5–labeled cortical MTs (magenta) in etiolated hypocotyl cells. MTs were severed by a 532-nm pulsed laser. The area of photo-ablation is indicated by the dotted-line and green lightning bolt. Images were acquired at 2-s intervals.

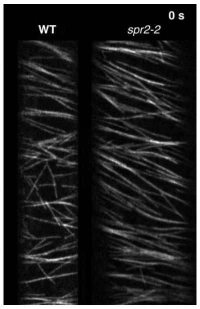

Video 6. **Time-lapsed images showing comparison of cortical MT array reorientation in etiolated hypocotyl cells of WT and *spr2-2* mutant seedlings stimulated by blue light perception.** Array reorientation in *spr2-2* is significantly inhibited. MTs are labeled with mCherry-TUA5. Images were acquired at 5-s intervals.

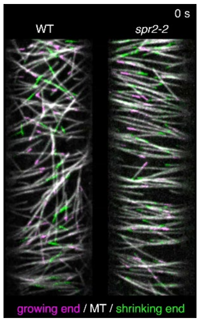

Video 7. **Time-lapsed imaging of cortical MT arrays in etiolated hypocotyl cells of WT and *spr2-2* mutant seedlings expressing mCherry-TUA5.** Image processing using a time-phased subtraction (Materials and methods) was used to detect growing and shrinking ends, displayed here as magenta and green comets, respectively. Highlighting growth and shrinkage in this way is a useful aid for visualizing MT-end dynamics. Images were acquired at 5-s intervals.

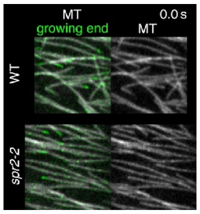

Video 8. **Example of image series of cortical MTs in WT and *spr2-2* dark-grown hypocotyl cells showing crossovers detected (yellow + signs) used for quantitative analysis.** MTs are labeled with mCherry-TUA5. Images were acquired at 5-s intervals. All the identified crossovers are marked with yellow + signs. Growing plus ends are shown in green.

Provided online is Table S1 in Excel, showing model input parameters.